RSC Advances

ROYAL SOCIETY OF CHEMISTRY

www.rsc.org/advances

Journal Name

ARTICLE

L-cysteine tailored porous graphene aerogel for enhanced power generation of microbial fuel cells

Received 00th January 20xx,
Accepted 00th January 20xx

DOI: 10.1039/x0xx00000x

www.rsc.org/

Yan Qiao[†]*[abc], Guo-Yun Wen[†abc], Xiao-Shuai Wu[abc], Long Zou[abc]

Graphene aerogel prepared from solution is a good candidate for microbial fuel cell (MFC) anode as it possesses three dimensional porous structure for high biocatalysts loading amount. However, the surface modification and pore size adjusting are always required during the synthetic process. In this work, we develop a highly biocompatible porous graphene aerogel from a one-pot synthesis with L-cysteine as the reductant. The addition of L-cysteine not only can reduce the graphene oxide at around 80 °C in atmosphere but also can tailor the pore size and structure of the aerogel. With the optimized ratio of L-cysteine in precursors, the obtained graphene aerogel G_{III} exhibits highly hydrophilic surface and appropriate pore structure for bacteria swimming in and adhesion. Increasing loading of bacteria cells on G_{III} anode enable it to achieve a maximum power density of 679.7 mW m^{-2} that is around 1.6-fold higher than the graphene aerogel prepared with hydrothermal method. This work provides a new way to prepare three-dimensional porous biocompatible anode material for improving the MFC performance.

1 Introduction

Microbial fuel cell (MFC) is capable of converting chemical energy stored in organic fuels including organic wastes directly into electrical energy by biocatalysts[1-5]. It has gained great interest as a renewable energy source and has been applied in many fields, particularly in wastewater treatment[6,7] and biosensors[8-11]. However, the relatively poor energy conversion efficiency and the low power density limit its practical applications. A lot of factors affect MFC performance, such as chemical substrate, cell internal, external resistance，proton exchange material, electrode spacing, and electrode materials[12-16]. Among these factors, the anode is generally considered as the main limiting factor for the low power density, which is mainly due to low bacteria loading onto the anode surface and low extracellular electron transfer efficiency between bacterial cells and electrode [17-19]. Thus, to explore superior anode materials is very critical for facilitating the bacteria adhesion and the interfacial electron transfer, which is attracting considerable attentions.

To improve the power output of MFCs, three-dimensional porous anodes have been applied such as reticulated vitreous carbon[20], graphite fiber brush[21], carbon nanotube coated textile or sponges[22], and polypyrrole or carbon nanotube-coated carbon foam[23]. Compared with the conventional flat anodes, the three-dimensional anodes provide larger surface area for bacteria adsorption and extracellular electron transfer. Among these 3D porous materials, self-assembled 3D graphene aerogels possess both structural merits and unique properties inherited from graphene sheets. In recent years, graphene has been adopted in MFC anodes to improve their performance owing to its extraordinary properties, including simple synthesis process, extremely high specific surface area, outstanding electrical conductivity, chemical inertness, and outstanding biocompatibility[24-27]. He et al. have demonstrated that hierarchically porous chitosan/vacuum-stripped graphene scaffold with the ISISA technique could increase the adhesion of bacteria and enhance the affinitive contact between multi-layered bacteria and biocompatible VSG[28]. In another work, a novel 3D structure graphene/PANI MFC anode could achieve a maximum about 4 times higher than that of the carbon cloth anode[29]. However, the synthetic procedures in these reports are quite complex so that it is not easy to tailor the pore size.

So far various kinds of methods have been used for graphene aerogel synthesis[30-32] and hydrothermal reduction is the mostly used method to prepare graphene aerogel from solution. However, the obtained aerogel often possesses quite hydrophobic surface that is hard for the electrolyte access. Further, the pore size is not enough for the bacteria cells move in so that the loading of biocatalysts cannot be further improved. It requires a simple strategy to tailor the pore size of

[a] Faculty of Materials and Energy, Southwest University, Chongqing 400715, P.R. China
[b] Institute for Clean Energy & Advanced Materials, Southwest University, Chongqing 400715, P.R. China
[c] Chongqing Key Laboratory for Advanced Materials and Technologies of Clean Energies, Chongqing 400715, P.R. China. Emali: yanqiao@swu.edu.cn
† Yan Qiao and Guo-Yun Wen contributed equally to this work.
Electronic Supplementary Information (ESI) available: [details of any supplementary information available should be included here]. See DOI: 10.1039/x0xx00000x

the graphene aerogel and generate a hydrophilic and biocompatible surface.

In this work, L-cysteine was used as reductant to prepare the graphene aerogel from solution at lower temperature (80 ° C) and atmosphere. The addition of L-cysteine can tailor the pore size and structure of the aerogel with an environmental-friendly method. It has been used to reduce[33] or modify[34] the graphene oxide nanosheets to increase the biocompatibility. The addition of L-cysteine environmental-friendly can tailor the pore size and structure of the aerogel. With the optimization of L-cysteine ratio in precursors, the graphene aerogel with appropriate pore size exhibits great bioelectrocatalytic performance.

2 Experimental

2.1. Preparation of graphene oxide

The graphene oxide (GO) used in this work was synthesized from graphite by a modified Hummers method[32]. In a typical preparation, 35mL of concentrated sulfuric acid (H_2SO_4) was added into a 250mL flask filled with 1 g of graphite , followed by the addition of 0.6g of sodium nitrate ($NaNO_3$). After ultrasonication and stirring for 30min in an ice bath, 4.5g of potassium permanganate ($KMnO_4$) was added under vigorous stirring. After continuously stirring the mixture at room temperature overnight, 36mL of deionized (DI) water was slowly added under vigorous agitation. The diluted suspension was kept at 50°C and stirred for one day. Finally 12mL of 30wt% H_2O_2 was added to the mixture. The mixture was then washed and centrifuged with 5wt%HCl and deionized water for several times until the pH of the mixture changed to neutral. The final GO colloid was obtained after 3h of ultrasonic treatment.

2.2 Preparation of graphene aerogels

In a typical preparation, 1.5 mg mL^{-1} GO dispersion was prepared with 50mL of deionized water under vigorous ultrasonication. After ultrasonication for 0.5h, L-cysteine was added and mixed well to chemically reduce and gelate the 2D GO sheets into a 3D graphene hydrogel. The concentration ratio of GO and L-cysteine was 1:1, 1:5, 1:13, 1:16 (the concentration of GO was constant in all samples). Then, the mixture was left in an oil bath at 80℃for 9h. Finally, the 3D structure was washed with deionized water several times and subsequently freeze dried for 24h to convert it into an aerogel. The obtained graphene aerogels are denoted as $G_{Ⅰ}$ (1:1), $G_{Ⅱ}$(1:5), $G_{Ⅲ}$ (1:13), $G_{Ⅳ}$(1:16).

To further investigate the effect of rGO with L-cysteine as reductant on the catalytic enhancement mechanism in MFCs, rGO was also obtained from the hydrothermal method. After 0.5h of ultrasonication, 30mL 1.5 mg mL^{-1} GO dispersion was transferred into a 50 mL Teflon-lined stainless steel autoclave, followed by heating the autoclave to 180 ℃ and kept for 12h. The obtained graphene aerogels are denoted as G_0.

2.3 Material characterization

Field emission scanning electron microscopy (FESEM, JSM-7800F, Japan) was used to investigate the morphology of electrode materials. X-Ray diffraction (XRD) spectra was recorded on a Shimadzu diffractometer (XRD-7000, Tokyo, Japan) with a scanning speed of 4° per minute. Infrared spectra were obtained with Fourier transform infrared spectroscopy (Nicolet 6700, FTIR, America). Nitrogen adsorption isotherms were measured with an automated gas sorption system (NOVA 1200e). The specific surface-area was calculated using Brunauer–Emmett–Teller (BET) method. Before examining the morphology, the discharged bacteria absorbed anodes were immersed in 4% polyoxymethylene overnight and then sequentially dehydrated with ethanol (30%, 40%, 50%, 60%, 70%, 80%, 90%, 100%) and dried in vacuum at room temperature for 12h.

2.4. Electrode preparation

The composite powders were mixed with PTFE solution. Then the mixture was coated on the surface of carbon cloth (1 cm×1cm) uniformly to prepare electrodes. After drying in vacuum at 100° C for 3h to remove water, the electrodes were used as anodes for MFCs.

2.5. MFC operation

A dual-chamber MFC was constructed using two glass flasks (with a volume of 100 ml). A proton exchange membrane (Nafion 117) was used to separate the cathode chamber and anode chamber. The area of anode was 1 cm^2 and the anolyte was M9 buffer (Na_2HPO_4, 6g L^{-1}; KH_2PO_4 , 3g L^{-1}; NH_4Cl , 1g L^{-1}; NaCl , 0.5g L^{-1}; $MgSO_4$, 1 mM； $CaCl_2$, 0.1 mM), which supplemented with 18 mM lactate as electron donor. *S. putrefaciens* cells was cultured under shaking at 30°C for 10h in lysogeny broth (LB) medium which was a mixture of 10g L^{-1} sodium chloride, 10g L^{-1} tryptone, and 5 g L^{-1} yeast extract. Subsequently, the bacterial was harvested by centrifuging at 6000 rpm (4°C, 5 min) and inoculated into a fresh lactic acid salt medium. For MFC operation, the above medium was transferred to the anodic chamber and purged with nitrogen for 30 min to remove oxygen. The external resistance for the discharge experiments was 1.5kΩ. The power curves and polarization curves were measured by varying the external load resistor from 0.1k Ω to 10k Ω to obtain a stable current. The cathode chamber contained 50mM potassium ferricyanide in 0.1 M phosphate buffered saline (pH 7.4).

2.6. Electrochemical measurements

The electrochemical analyses were performed with in a three-electrode model that consisted of the working electrode, an SCE as the reference electrode and a carbon cloth (2cm × 2cm) as the counter electrode. Cyclic voltammograms (CVs) and electrochemical impedance spectroscopy (EIS) experiments were conducted by using a potentiostat (CHI660E, Shanghai Chenhua, China). For the measurement in M9 buffer and lactic acid salt medium, the bacteria was washed with M9 buffer and lactic acid salt medium to remove the adsorbed lysogeny broth (LB) medium respectively. Electrochemical impedance measurements of the rGO electrodes were

Journal Name

ARTICLE

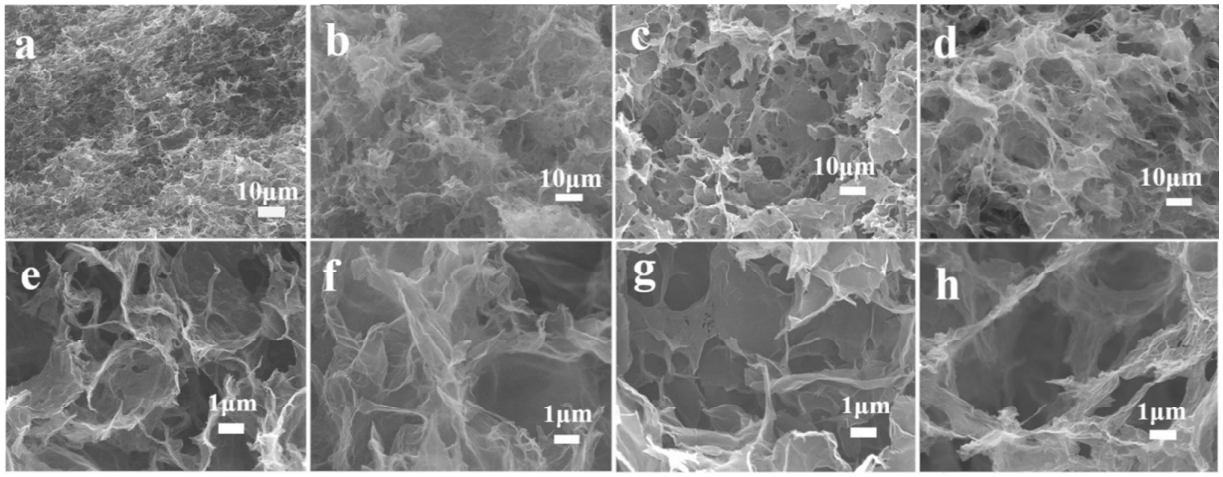

Fig. 1. FESEM images of graphene aerogels prepared with different concentration ratio of GO and L-cysteine (b, f G_{II} 1:5, c, g G_{III} 1:13, d, h G_{IV} 1:16). (a, e): SEM image of G_0

performed at -0.45V vs. SCE over a frequency range of 0.01 Hz to 100 KHz with sinusoidal perturbation amplitude of 5mV. All tests were conducted at room temperature.

3 Results and discussion

3.1. Characterization of graphene aerogels

The morphologies of graphene aerogels prepared under different conditions were examined by FESEM at different magnifications, as shown in Fig. 1 and Fig. S1. It is worth noting that the graphene aerogels have a self-assembled 3D interconnected structure with macropores. The introduction of L-cysteine apparently enlarge the pore size of the graphene aerogels. As the increasing ratio of L-cysteine, the pore size is enlarged more (Fig. S1, Fig.1c-h). When the GO to L-cysteine ratio increases to 1:13, the aerogel (Fig.1c, g) still can maintain the uniform porous structure. However, when the GO to L-cysteine ratio increases to 1:16 (Fig.1d, h), the pore size is over enlarged so that the porous structure almost cracks up.

X-ray diffraction measurements were used to investigate the structure and crystal phase of the synthesized composites. For the GO sample, the sharp peak at around 2 θ = 10.4° corresponding to the (002) reflection of exfoliated GO is observed (Fig.S2a). As shown in Fig.2a, after hydrothermal or oil bath treatment, this peak disappeared and a broad peak at about 2 θ = 24.6° appeared, indicating the reduction of GO to rGO. The diffraction peaks presented in the patterns of G_{II}, G_{III} and G_{IV} are corresponding to cystine (PCPDF No. 37-1802). This suggests that the L-cysteine is oxidized to cystine and remains in these graphene aerogels.

In addition, the specific surface area of graphene aerogels was measured with N2 adsorption /desorption methods. Apparently, no big difference of the specific surface area is observed for L-cysteine reduced graphene aerogels (Fig. S3a). Moreover, the specific surface area of G_0 is larger than other graphene aerogels reduced by L-cysteine, which could possibly be attributed to the enlarged pores by L-cysteine (Fig. S3b). Most noticeably, the isotherms have hysteretic loops that are characteristics of the adsorption–desorption of mesoporous material. Moreover, the results clearly indicate that the dominant pore size of the aerogels is around 35nm (the inset of Fig. S3).

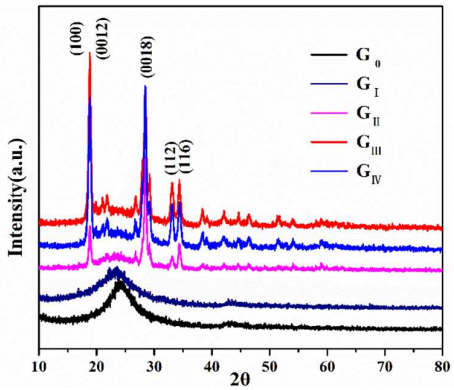

Fig. 2. XRD of graphene aerogels prepared with different concentration ratio of GO and L-cysteine (G_0, G_I, G_{II}, G_{III}, G_{IV})

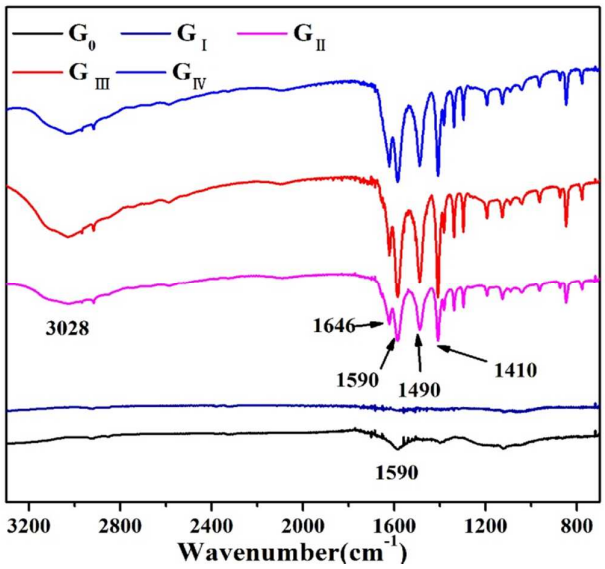

Fig. 3. FTIR spectra of graphene aerogels

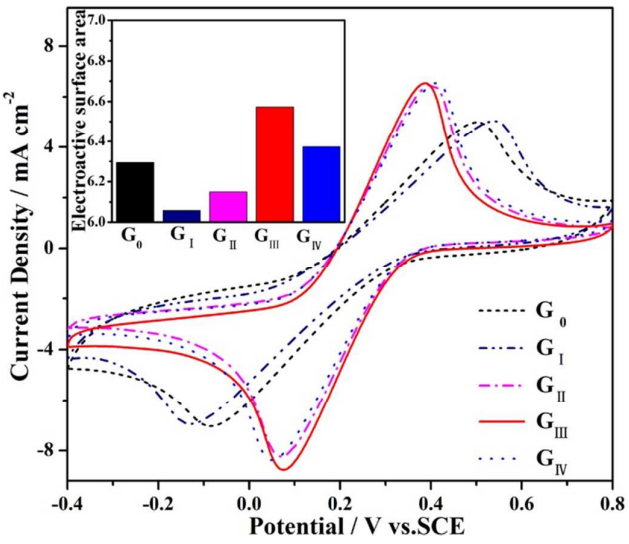

Fig. 4. Electrochemical characterization of graphene aerogels by cyclic voltammograms with a scan rate of 5 mV s^{-1} in potassium ferricyanide solution

In GO reduction process, the self assembly of GO sheets is due to the removal of electrostatic repulsion from the ionization of the oxygen-containing groups and the increase of attractive interaction of the van der Waal force from the carbon framework when the GO is reduced. For the hydrothermal reduction, a continuous liquid phase behaves as the spacer to help the formation of the interlinked pore structure[27]. While for the L-cysteine reduction, the cystine containing amino group and carboxyl group remains on the rGO surface may work as the spacer to enlarge the pores of the aerogel (Fig. S4).

Fig. 3 presents the FT-IR spectra of GO after reduction by different methods. For the GO sample, the stretching vibration of O-H shows at 3430 cm^{-1}, and the characteristic peaks for C=O stretching vibration appear at 1740cm^{-1}. Aromatic C=C stretching vibration appears at 1625 cm^{-1}, and the peaks at 1220 cm^{-1} can be assigned to the epoxy C–O stretching vibration (Fig. S2b). While being reduced by hydrothermal and L-cysteine (G_I), the peaks for oxygen functional groups disappeared completely. As the increasing ratio of L-cysteine, the peaks for oxygen functional groups of the composite obtained can be observed clearly. As shown in Fig. 3, the broad and strong peak near 3028 cm^{-1} indicates the stretching vibrations of O-H in the carboxyl group. In addition, the peaks at 1646cm^{-1} and 1590cm^{-1}can be attributed to the -NH bending vibration and C=C stretching vibration, respectively. The peak around 1410cm^{-1} results from the stretching vibrations of the C-O in the carboxyl group and the peak at 1490 cm^{-1} is due to the O-H bending vibration. These results are in a good agreement with the XRD patterns. It is worth noting that the function groups from the cystine will increase the surface hydrophilicity of the graphene aerogels for electrolyte access and bacteria cells adhesion. To prove this, the water contact angles of G_0 and G_{III} were measured (Fig. S5). The results suggest that G_0 has a quite hydrophobic surface (the water contact angle is 86.63°), while G_{III} has a hydrophilic surface (the water contact is 27.98°).

The electroactive surface areas of graphene aerogel electrodes which was calculated according to the redox peak area of CV curves[26] were evaluated in 0.05M $K_3[Fe(CN)_6]$ with 1 M phosphate buffered saline (PBS) solution. The electroactive surface area, which was reported in literature1. As displayed in Fig. 4, cyclic voltammograms (CVs) of G_{II}, G_{III}, G_{IV} show a pair of well-defined $[Fe(CN)_6]^{3-}/[Fe(CN)_6]^{4-}$ redox waves while the CV curve of G_0 and G_I are distorted obviously. It could be due to the improved hydrophilicity of cystine functionalized graphene aerogels enhances the interfacial charge transfer rate. The maximum redox peak current is obtained at the G_{III} electrode, which suggests the largest active surface area for access of the ferricyanide ions. Considering the poor reversibility of G_I, it were not used in following electrocatalytic analysis.

3.2. Electrocatalytic performance of the graphene aerogel anodes

The electrocatalytic analysis of G_0, G_{II}, G_{III} and G_{IV} electrodes were investigate in M9 buffer, M9 buffer with suspended *S. putrifeciens* cells and *S. putrefaciens* cells suspensions in lactic acid medium respectively. It is noted that the G_{III} electrode has the largest capacitive current, which is in accordance with the electroactive surface area investigated in potassium ferricyanide solution (Fig. 5a). To further investigate the electrocatalytic performance of the graphene aerogel electrodes, cyclic voltammograms and electrochemical impedance spectra were examined in anaerobically activated *S. putrefaciens* cells without lactate added in. As shown in Fig.5b, a weak redox pair can be found on each CV curve, which can be attributed to the trace amount of flavins generated by *S. putrefaciens* cells. As displayed in Fig 5c, a well defined redox pair can be observed at around -0.45V on each CV curve

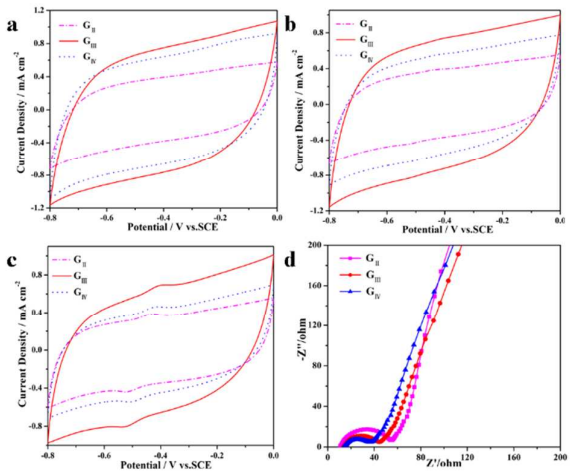

Fig. 5 Cyclic voltammograms conducted in M9 buffer (a), in M9 buffer with suspended *S. putrifeciens* cells (b), Cyclic voltammograms (c) with a scan rate of 30 mV s^{-1} and Nyquist plots (d) conducted in *S. putrefaciens* cells suspensions in lactic acid medium

indicating the redox reaction of flavins. To make it easier to observe the substract oxidation current, CVs with a scan rate of 1mV s^{-1} were conducted in *S. putrefaciens* cells suspensions in lactic acid medium (Fig. S6). Among the three electrodes, the G_{III} has much higher redox peak current than the other two electrodes (Fig.S7) and the capacitive current. As the specific surface area and the electroactive surface area of these three electrodes are similar, the maximum redox peaks achieved by G_{III} electrode could be due to the increased loading of *S. putrefaciens* cells, who can excrete more flavins on the electrode-bacteria interface. The Nyquist plots (Fig. 5d) exhibit that the G_{III} and G_{IV} possess faster interfacial charge transfer than G_{II}. The reason might be that the more remained cystine (refer to Fig. 2) make the surface of graphene sheets to be more hydrophilic for fast redox reaction.

In addition, the CV of G_0 electrode (Fig. S8) shows a high capacitive current, but no obvious redox waves can be observed. It could be due to the low Faraday current hided by high charge current density. The CV of G_{III} electrode shows much larger redox peak current in comparison to that of G_0 electrode. The improvement could be attributed to the remained cystine (refer to Fig. 2) make the surface of graphene sheets to be more hydrophilic (refer to Fig. S5) and appropriate pore structure. The EIS analysis shows that the R_{ct} of G_{III} electrode is lower than that of G_0 electrode.

To evaluate the performance of graphene aerogel anodes achieved in MFCs, the output current density of G_{III} and G_0 anodes were measured in dual-chamber configurations for four cycles (Fig.6a). As displayed in Fig.6a, the output current density of the MFC with G_{III} anode can achieve a plateau of 365μA cm^{-2} for 52 h, and then decreases sharply due to the exhaustion of the substrates. However, when the medium in the anode chamber was refreshed, the current density quickly recovered to a value as high as 318.8 μ A cm^{-2}. Furthermore,

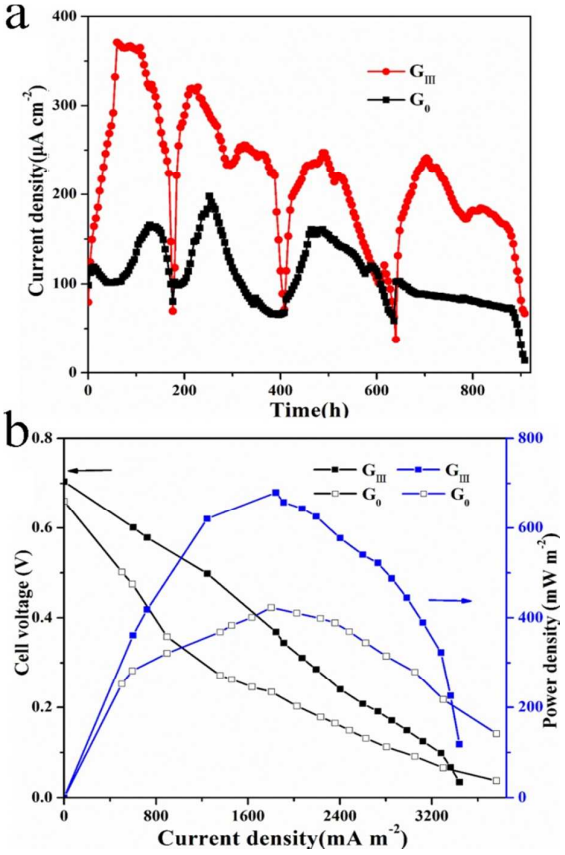

Fig. 6 Discharge performance (a), power curves and polarization curves (b) of MFCs with different anodes

the discharging curves show that the G_{III} anode generates higher current density than the G_0 anode. For the three L-cysteine tailored graphene aerogel anodes, G_{III} also delivers highest current density in each discharging cycle (Fig. S9). As the substrate concentration in both MFCs is same, the remarkable improvement indicates that the L-cysteine tailored graphene aerogel anodes deliver higher energy conversion efficiency. The L-cysteine not only tailored the porous structure of the graphene aerogel but also provide abundant functional groups to promote the bacteria adhesion as well as the electrolyte accesses. The output power density curves and polarization curves in Fig. 6b illustrate that the optimized G_{III} anode delivers a maximum power density of 679.7 mW m^{-2}, which is around 1.6-fold higher than that of the G_0 anode (422.86mWm^{-2}). The polarization curves in Fig.6b reveal that the G_{III} electrode has a much lower polarization for better energy conversion efficiency. Overall, these results demonstrate that the highly biocompatible porous graphene aerogel anode reduced with L-cysteine could greatly improve the power output performance of MFCs and can be a superior anode material in an MFC.

To comprehensively understand the catalytic enhancement in the MFCs, the surface morphology of the G_{III} anode were examined by FESEM after discharge. As shown in Fig.7, the bacterial cells not only adhered on the outside surface of the

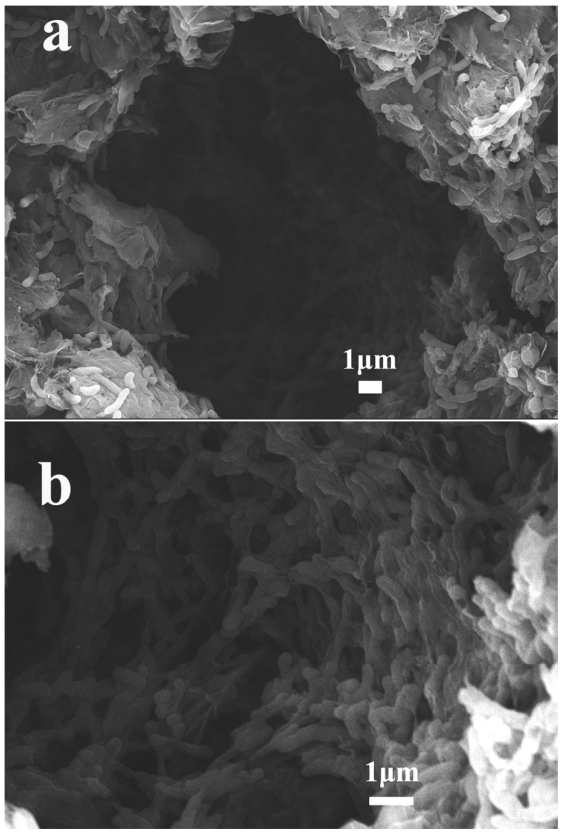

Fig.7 SEM micrographs of *S. putrefaciens* cells adhered on the G_{III} anode electrode surface

graphene aerogels but also colonized in the pores. Most noticeably, high resolution SEM image (Fig.7b) of the interior of the GIII anode reveals that the cells were densely adhered on the inside surface of the porous electrode and accumulated together to form a biofilm network. It is worth mentioning that this not only significantly improves the loading of the biocatalyst but also greatly facilitates electron transport between electrodes and bacterial cells. It is also noted that the thick biofilm might block the access of flavins from bulk solution to the electrode surface, which result in the slightly decrease of the current output plateau in cycle 2 - 3. However, the discharging time of cycle 4 is longer than cycle 3 while the current density is almost same. It could be due to the increased bacteria cells in the biofilm obtain more electrons from the substrate. Meanwhile, the image of the G_0 anode after discharge is displayed in Fig. S10 for comparison. Based on the image, the cell density on the G_0 anode surface is much lower than that of the G_{III} anode, in which only few cells were detected in the interior of the G_0 electrode. According to the all above physical and electrochemical analyses, the G_{III} composite not only possesses appropriate pore structure for bacteria cells move in and adhesion but also has large hydrophilic surface for electrolyte access and flavins redox reaction. That could be the reason for its superior catalytic performance in the MFC anode.

4 Conclusions

In a brief, a highly biocompatible porous reduced graphene oxide anode from a one-pot synthesis with L-cysteine as reductant was developed to simultaneously boost both electro- and bio-catalytic process for a high performance MFC. With the optimized ratio of L-cysteine in precursors, the obtained G_{III} has 3D porous structure to provide lots of active sites and also possesses hydrophilic and biocompatible surface for flavins redox reaction and bacterial attachment. This work not only provides a new strategy to prepare graphene aerogel with a simple and environmental-friendly way but also gives some insights to how to build a high bacteria loading anode for MFCs.

Acknowledgements

We gratefully acknowledge to the financial support from the Fundamental Research Funds for the Central Universities (XDJK2015B018), National Natural Science Foundation of China(No. 31200102), Institute for Clean Energy & Advanced Materials, Southwest University, Chongqing, P.R. China, Chongqing Key Laboratory for Advanced Materials and Technologies of Clean Energies.

Notes and references

‡ Footnotes relating to the main text should appear here. These might include comments relevant to but not central to the matter under discussion, limited experimental and spectral data, and crystallographic data.

1. S. Cheng and J. Wu, *Bioelectrochem.*, 2013, **92**, 22-26.
2. J. Sun, Y. Hu, Z. Bi and Y. Cao, *J. Power Sources*, 2009, **187**, 471-479.
3. Gnana kumar, C. J. Kirubaharan, S. Udhayakumar, C. Karthikeyan and K. S. Nahm, *Ind. Eng. Chem. Res.* , 2014, 53, 16883-16893.
4. G. G. Kumar, S. Hashmi, C. Karthikeyan, A. GhavamiNejad, M. Vatankhah-Varnoosfaderani and F. J. Stadler, *Macromol. Rapid Commun.*, 2014, 35, 1861-1865.
5. G. Gnana Kumar, Z. Awan, K. Suk Nahm and J. S. Xavier, *Biosens. Bioelectron.*, 2014, 53, 528-534.
6. Z. Du, H. Li and T. Gu, *Biotechnol. Adv.*, 2007, **25**, 464-482.
7. S. Venkata Mohan, R. Saravanan, S. V. Raghavulu, G. Mohanakrishna and P. N. Sarma, *Bioresour. Technol.*, 2008, **99**, 596-603.
8. G. Gnana kumar, K. Justice Babu, K. S. Nahm and Y. J. Hwang, *RSC Adv.*, 2014, 4, 7944.
9. I. S. Chang, H. Moon, J. K. Jang and B. H. Kim, *Biosens. Bioelectron.*, 2005, **20**, 1856-1859.
10. F. Golitsch, C. Bucking and J. Gescher, *Biosens. Bioelectron.*, 2013, **47**, 285-291.
11. I. S. Chang, J. K. Jang, G. C. Gil, M. Kim, H. J. Kim, B. W. Cho and B. H. Kim, *Biosens. Bioelectron.*, 2004, **19**, 607-613.
12. R. A. Bullen, T. C. Arnot, J. B. Lakeman and F. C. Walsh, *Biosens. Bioelectron.*, 2006, **21**, 2015-2045.
13. K. Rabaey and W. Verstraete, *Trends biotechnol.,* 2005, **23**, 291-298.
14. H. S. Park, B. H. Kim, H. S. Kim, H. J. Kim, G. T. Kim, M. Kim, I. S. Chang, Y. K. Park and H. I. Chang, *Anaerobe*, 2001, **7**, 297-306.

15. C. S. Butler and R. Nerenberg, *Appl. Microb. Biotech.*, 2010, **86**, 1399-1408.
16. B. E. Logan and M. Elimelech, *Nature*, 2012, 488, 313-319.
17. G. Reguera, K. P. Nevin, J. S. Nicoll, S. F. Covalla, T. L. Woodard and D. R. Lovley, *Appl. Environ. Microbiol.*, 2006, 72, 7345-7348.
18. G. Reguera, K. P. Nevin, J. S. Nicoll, S. F. Covalla, T. L. Woodard and D. R. Lovley, *Appl. Environ. Microbiol.* , 2006, 72, 7345-7348.
19. Y. Yuan, S. Zhou, Y. Liu and J. Tang, *Environ. Sci. Techno.*, 2013, **47**, 14525-14532.
20. Z. He, S. D. Minteer and L. T. Angenent, *Environ. Sci. Techno.*, 2005, **39**, 5262-5267.
21. B. Logan, S. Cheng, V. Watson and G. Estadt, *Environ. Sci. & Techno.*, 2007, **41**, 3341-3346.
22. X. Xie, M. Pasta, L. Hu, Y. Yang, J. McDonough, J. Cha, C. S. Criddle and Y. Cui, *Energ. Environ. Sci.*, 2011, **4**, 1293-1297.
23. Y. Yuan and S. Kim, *Bull. Korean Chem. Soc.*, 2008, **29**, 168.
24. Y.-C. Yong, X.-C. Dong, M. B. Chan-Park, H. Song and P. Chen, *ACS nano*, 2012, **6**, 2394-2400.
25. J. Liu, Z. He, J. Xue and T. T. Y. Tan, *J. Mater. Chem. B*, 2014, **2**, 2478-2482.
26. Y. Qiao, X.-S. Wu, C.-X. Ma, H. He and C. M. Li, *RSC Adv.*, 2014, **4**, 21788-21793.
27. Y.-X. Huang, X.-W. Liu, J.-F. Xie, G.-P. Sheng, G.-Y. Wang, Y.-Y. Zhang, A.-W. Xu and H.-Q. Yu, *Chem. Comm.*, 2011, **47**, 5795-5797.
28. Z. He, J. Liu, Y. Qiao, C. M. Li and T. T. Y. Tan, *Nano Lett.*, 2012, **12**, 4738-4741.
29. S. Pei and H.-M. Cheng, *Carbon*, 2012, **50**, 3210-3228.
30. J. Zhang, H. Yang, G. Shen, P. Cheng, J. Zhang and S. Guo, *Chem. Comm.*, 2010, 46, 1112-1114.
31. H. Wei, M.-W. Xu, S.-J. Bao, F. Yang and H. Chai, *RSC Adv.*, 2014, 4, 16979-16984.
32. D. Chen, L. Li and L. Guo, *Nanotechnology*, 2011, 22, 325601.
33. J. Zhang, Z. Xiong and X. Zhao, *J. Mater. Chem.*, 2011, 21, 3634-3640.
34. W. Lv, C. Zhang, Z. Li and Q.-H. Yang, *J. Phys. Chem. Lett.*, 2015, 6, 658-668.